

Update feasibility studies of time-like proton electromagnetic form factors at $\overline{\text{PANDA}}$ -FAIR

Author¹

Institut

Received: date / Revised version: date

Abstract. the red color along the text underlines the parts that have to be updated The results of simulations for future measurements of electromagnetic form factors at $\overline{\text{PANDA}}$ (FAIR) in frame of the PANDARoot software are reported. The statistical precision at which the proton form factors can be determined is estimated. The suppression of the main background ($\bar{p}p \rightarrow \pi^+\pi^-$) process versus the signal ($\bar{p}p \rightarrow e^+e^-$) efficiency, the extraction of the information from the relevant spectra and the evaluation of the statistical errors on the extracted proton FF ratio from the events of the reaction $\bar{p}p \rightarrow e^+e^-$ have been done on the basis of two different but consistent procedures. The procedure developed here will be directly applied to the experimental data. The comparison with older predictions based on BABAR framework shows consistency of the results and a slightly better precision achieved in a large range of momentum transfer, assuming the nominal conditions of beam and detector performances (?).

PACS. 25.43.+t Antiproton-induced reactions – 13.40.Gp Electromagnetic form factors

1 Introduction

The $\overline{\text{PANDA}}$ [32] experiment at FAIR (Darmstadt) will detect the products of the annihilation reactions induced by high intensity antiproton beams with momentum ranging from 1.5 to 15 GeV/c. The broad physics program includes charmonium spectroscopy, search for hybrids, glueballs, charm and strangeness in nuclei, as well as nucleon structure studies [42]. Here we focus on the extraction of time-like (TL) proton electromagnetic form factors (FFs) through the measurement of the angular distribution of the electron(positron) in the annihilation into an electron-positron pair.

Electromagnetic FFs of hadrons are fundamental quantities which describe their intrinsic electric and magnetic distributions. In the TL region they have been associated to the time evolution of these distributions [27].

Theoretically, they enter in the parametrization of the proton electromagnetic current. They are experimentally accessible through measurements of cross sections and angular distributions for elastic ep scattering in the space-like (SL) region and $\bar{p} + p \leftrightarrow e^+ + e^-$ in the TL region, assuming that the interaction occurs through the exchange of one-photon, which carries a momentum transfer squared q^2 (corresponding to the total energy squared s in TL region).

Although measurements exist since decades [24], recently the possibility to apply the polarization method [3, 4] and to access with high precision a wide kinematical range, arised new interest and new questions in the field. The data from the JLab-GEp collaboration up to a value

of the momentum transfer squared of $Q^2 = -q^2 = 8.9$ GeV² showed that the electric and magnetic distributions inside the proton are not the same, contrary to what previously assumed: the ratio of the electric to the magnetic FF, $\mu_p G_E/G_M$ (μ_p is the anomalous proton magnetic moment) decreases almost linearly from unity as the momentum transfer squared increases, approaching a zero value.

In the TL region, the individual determination of FFs is more difficult as it has been limited by the luminosity of the e^+e^- and $\bar{p}p$ colliders. Attempts have been done at LEAR and more recently by BABAR using initial state radiation (ISR). The FF ratio shows different trend, somehow inconsistent in the limit of the errors and definitely calls for more precise experiments.

The $\overline{\text{PANDA}}$ experiment, designed with a maximum luminosity of $\mathcal{L} = 10^{-32} \text{cm}^{-2} \text{s}^{-1}$, will bring new information in two respects: the measurement of the angular distribution for the individual determination of FFs, and the measurement of the integrated cross section for the extraction of a generalized FF up to larger values of s . These data are expected to constitute a stringent test of nucleon models. In particular the high s region brings information on analyticity properties of FFs and on the asymptotic q^2 behavior predicted by QCD.

The FAIR facility is in the construction phase and the $\overline{\text{PANDA}}$ experiment is planning to start taking data at the end of 2018(?). Simulations for the different physics processes have been done or are in progress. The feasibility of the FFs measurement with the $\overline{\text{PANDA}}$ detector, as suggested in [38], has been investigated in Ref. [36]. The necessity to update that work is due to the fact that

these first estimations were done in the "Babar framework" i.e., adapting the programmes of the BABAR experiment to a simplified version of the $\overline{\text{PANDA}}$ detector. Since then, large progress in the design of the detector has been achieved. Prototypes for parts of subdetectors have been built. Data under test beams have been collected and analyzed for prototypes, suggesting improvement in the design. The Technical Design Reports for most of the detectors are publically available. Although the analysis program is still in progress, in parallel with the detector construction, a realistic description of the subdetectors and new algorithms for the tracking have been implemented. **more specific here** More specifically, in the BABAR framework, the $\overline{\text{PANDA}}$ geometry does not contain a complete description of large part of the detection: a detector may be replaced by the effect of its acceptance and resolution. In the case of the muon detector the geometry was inadequate and, for example, the simulations of the Drell-Yan process in [32] have required a different framework. The tracking for the barrel as well as for the forward spectrometer was ideal and the pattern recognition unrealistic. Moreover, during the recent years GEANT4 has undergone continuous improvement, and most of the known bugs have been fixed since.

In the present version of PANDARoot let us stress in particular, that the description of most of the subdetectors has been completed with passive materials, pipe, magnet yoke... A realistic mapping of the magnetic field, calculated with TOSCA has been implemented, as well as the digitization extracted from experimental data. The pattern recognition for forward tracking has essentially improved.

The aim of this paper is to present a new simulation, based on the most recent version of PANDARoot available (version...) in order to check the validity of the assumptions previously used and confirm the feasibility of the e^+e^- detection at a sufficient level of precision. Moreover a new and efficient analysis tool has been developed, which will be applied to the treatment of the experimental data. Lastly, the generation of a huge number of events has allowed a full scale operation of the PANDAGRID, and of the HIMSTER cluster, stimulating the optimization of the necessary procedures to collect, save, stock and transfer a large amount of Monte Carlo data, which have the same structure as the expected physics data.

to be updated following the paper

The plan of the paper is the following. The kinematics of the reactions of interest (signal and background) and the evaluation of the counting rates is done in section 2. The detector is briefly described in Section 3. The standard chain of the full simulation with PANDARoot and the procedure to identify and analyze the signal and the background, based on the properties of the kinematics and the PID information from the sub-detectors, are described in section 4. Finally, the results on the angular asymmetry $\mathcal{A} \pm \Delta\mathcal{A}$ and on the proton FF ratio $R \pm \Delta R$ are presented in section 5 as well as the error on the effective FFs. Conclusions contain a summary and final remarks.

2 Basic formalism

Let us consider the reactions:

$$\bar{p}(p_1) + p(p_2) \rightarrow h^-(k_1) + h^+(k_2), \quad h = e, \mu, \pi, \quad (1)$$

where the four-momenta of the particles are written in parentheses. The analysis is mainly done in Center of Mass (CM) system, where the four-momenta are:

$$\begin{aligned} p_1 &= (E, \mathbf{p}), \quad p_2 = (E, -\mathbf{p}), \\ k_1 &= (E, \mathbf{k}), \quad k_2 = (E, -\mathbf{k}), \quad \mathbf{p} \cdot \mathbf{k} = pk \cos \theta, \end{aligned} \quad (2)$$

θ is the angle between the negative emitted particle and the antiproton beam.

The cylindrical symmetry of the unpolarized binary reactions around the beam axis originates an isotropic distribution in the azimuthal angle ϕ . These reactions are two body final state processes. The final particles in the pair are emitted back to back in the CM system and each of them, having equal mass, carries half of the total energy of the system, $E = \sqrt{s}/2$, where the invariant s is $s = q^2 = (p_1 + p_2)^2 = (k_1 + k_2)^2$.

All leptons in the final state (e, μ, τ) bring the same physical information on the electromagnetic hadron structure. However, the experimental requirements for their detection are peculiar to each particle species. In this work we focus on the electron pair production, denominated *the signal* and on the charged pion pair production, denominated *the background*. The production of a charged pion pair is 10^6 times more probable compared to a e^+e^- pair. The signal and the background have very similar kinematics because the mass of the electron is sufficiently close to the pion mass. Therefore the kinematics plays a minor role in the electron/pion separation. The kinematical selection helps for the suppression of the hadronic contribution related to the channels with more than two particles in the final states, or secondary particles which come from the interaction of primary particles with the detector material. Kinematical selection is also very effective in eliminating neutral pions, as it has been discussed in [36,23]. Note that the $\pi^0\pi^0$ cross section is ten times smaller compared to $\pi^+\pi^-$.

2.1 The signal

The expression of the hadron electromagnetic current for the $\bar{p}p$ annihilation in two leptons is derived assuming one photon exchange (OPE). The internal structure of the hadrons is then parametrized in terms of two FFs, which are complex functions of q^2 , the four momentum squared of the virtual photon. For the case of unpolarized particles the differential cross section has the form [44]:

$$\frac{d\sigma}{d\cos\theta} = \frac{\pi\alpha^2}{2\beta s} \left[(1 + \cos^2\theta)|G_M|^2 + \frac{1}{\tau} \sin^2\theta|G_E|^2 \right],$$

$$\beta = \sqrt{1 - \frac{1}{\tau}}, \quad \tau = \frac{s}{4m^2}$$

or in equivalent form:

$$\frac{d\sigma}{d\cos\theta} = \sigma_0 [1 + \mathcal{A} \cos^2 \theta], \quad (3)$$

where σ_0 is the value of the differential cross section at $\theta = \pi/2$ and \mathcal{A} is an angular asymmetry which can be written as a function of the FFs:

$$\begin{aligned} \sigma_0 &= \frac{\pi\alpha^2}{2\beta s} \left(|G_M|^2 + \frac{1}{\tau} |G_E|^2 \right) \\ \mathcal{A} &= \frac{\tau |G_M|^2 - |G_E|^2}{\tau |G_M|^2 + |G_E|^2} = \frac{\tau - \mathcal{R}^2}{\tau + \mathcal{R}^2}, \end{aligned} \quad (4)$$

where $\mathcal{R} = |G_E|/|G_M|$.

This form has several advantages:

- considering σ_0 and \mathcal{A} the parameters to be extracted from the experimental angular distribution, the fit function reduces to a linear function (instead than quadratic);
- \mathcal{A} lies in the range $-1 \leq \mathcal{A} \leq 1$.

Therefore it is expected to reduce instabilities and correlations in the fitting procedure. Note that in real experiments, the angular range where the measurement can be performed is usually restricted to $|\cos\theta| \leq \bar{c}$ with $\bar{c} = \cos\theta_{max}$. The integrated experimental cross section is

The integrated experimental cross section is

$$\begin{aligned} \sigma_{int} &= \int_{-\bar{c}}^{\bar{c}} \frac{d\sigma}{d\cos\theta} d\cos\theta = \frac{2}{\sigma_0} \bar{c} \left(1 + \frac{\mathcal{A}}{3} \bar{c}^2 \right) \\ &= \frac{\pi\alpha^2}{2\beta s} \bar{c} \left[\left(1 + \frac{\bar{c}^2}{3} \right) |G_M|^2 + \frac{1}{\tau} \left(1 - \frac{\bar{c}^2}{3} \right) |G_E|^2 \right] \end{aligned} \quad (5)$$

Note that in real experiments, the angular range where the measurement can be performed is usually restricted to $|\cos\theta| \leq \bar{c}$ with $\bar{c} = \cos\theta_{max}$. The total cross section corresponds to $\bar{c} = 1$:

$$\sigma_{tot} = 2\sigma_0 \left(1 + \frac{\mathcal{A}}{3} \right) = \frac{2\pi\alpha^2}{3\beta s} \left[2|G_M|^2 + \frac{|G_E|^2}{\tau} \right]. \quad (6)$$

One can define an effective form factor from the **total** cross section by

$$|F_p|^2 = \frac{3\beta s \sigma_{tot}}{2\pi\alpha^2 \left(2 + \frac{1}{\tau} \right)}. \quad (7)$$

or from the **integrated** cross section by

$$|F_p|^2 = \frac{\beta s}{\pi\alpha^2} \frac{\sigma_{int}}{\bar{c} \left[\left(1 + \frac{\bar{c}^2}{3} \right) + \frac{1}{\tau} \left(1 - \frac{\bar{c}^2}{3} \right) \right]}. \quad (8)$$

which is equivalent to the value extracted from cross section measurements assuming $|G_E| = |G_M|$, as usually done in the literature.

Different parametrizations of hadron FFs, which are inspired by different descriptions of the internal electromagnetic structure of the proton, can be found in the literature. In Fig. 1 the world data are illustrated, together

with few parametrizations. In Ref. [36] two parametrizations were considered. The parameters were fitted on the experimental data of the known integrated experimental cross section. Since, new data from BABAR have been made available ([31,30]).

The QCD inspired parameterization of $|G_{E,M}|$ is based on analytical extension of the dipole formula to TL region and corrected to avoid 'ghost' poles in α_s (the strong interaction running constant) [34]:

$$|G_{E,M}^{QCD}| = \frac{A}{s^2 [\log^2(s/\Lambda^2) + \pi^2]}, \quad (9)$$

where $A^{QCD} = 89.45$ [GeV/c]⁴. is obtained fitting the experimental data and $\Lambda = 0.3$ GeV is the QCD scale parameter. It is shown as a blue dash-dotted line. One can see that the new data from BABAR at large s , ([30]), suggest a steeper decrease which can not be reproduced with the s dependence from 9.

The parametrization (10) adds an additional s -power in the denominator, with respect to dipole [37]:

$$|G_M| = \frac{A}{1 + s [GeV^2]/m_a^2} G_D, \quad G_D = (1 + s [GeV^2]/0.71)^{-2}. \quad (10)$$

where s is expressed in [GeV²]. It is illustrated as a black solid line with the nominal parameters $A = 22.5$ and $m_a^2 = 3.6$ GeV². Note that an updated global fit with a data set including 85 points (starting from $s=4$. GeV²) gives $A(fit) = 71.5$ and $m_a^2(fit) = 0.85$ GeV², with a value of $\chi^2/ndf = 1.4$ (red dashed line), overestimating the low energy data. These parametrizations reproduce reasonably well the data in the considered kinematical region. For the present evaluations, we chose the parametrization (10) with the nominal parameters.

The expected counting rates are tabulated in Table 1, assuming $R = G_E/G_M = 1$, the parametrization from Eq. (10) and the angular range $|\cos\theta| \leq 0.8$. For each kinematical point the first line corresponds to an integrated luminosity of 2 fb⁻¹ (i.e., four months of measurement with 100% efficiency at the maximum luminosity of $\mathcal{L} = 2 \cdot 10^{32}$ cm⁻²s⁻¹) and the second line to a reduced luminosity by a factor of ten.

2.2 The background

In order to estimate the $\pi^+\pi^-$ background in the interesting kinematical range, phenomenological parametrizations have been developed and a dedicated generator as been built (see Ref. [43] and references therein).

The difficulties for a consistent physical description are related to different aspects:

- the most probable reaction mechanism is changing with the energy and the angle,
- data are very scarce not allowing to constrain parameter models.
- model independent considerations based on crossing symmetry or T-invariance, which may help to find constrain from the related reactions, can not be considered as predictive [35].

s [GeV/c] ²	p [GeV/c]	$\sigma_{int}(e^+e^-)$ [pb]	$N_{int}(e^+e^-)$	$\sigma_{int}(\pi^+\pi^-)$ [μb]	$N_{int}(\pi^+\pi^-)$ $\cdot 10^{-6}$	$\frac{\sigma_{int}(\pi^+\pi^-)}{\sigma_{int}(e^+e^-)}$
5.4	1.7	417.39	$83.48 \cdot 10^4$ $83.48 \cdot 10^3$	101.06	$202.12 \cdot 10^9$ $202.12 \cdot 10^8$	0.24
8.2	3.3	24.61	$49.21 \cdot 10^3$ $49.21 \cdot 10^2$	2.95	$5.9 \cdot 10^9$ $5.9 \cdot 10^8$	0.12
13.8	6.3	0.77	1538.16 153.82	0.16	$3.18 \cdot 10^8$ $3.18 \cdot 10^7$	0.21
*16.7	7.9	$21.35 \cdot 10^{-2}$	426.93 42.69	0.05	$*10.05 \cdot 10^7$ $10.05 \cdot 10^6$	0.24*
*22.3	10.9	$30.22 \cdot 10^{-3}$	60.43 6.04	0.01	$2.05 \cdot 10^7$ $*2.05 \cdot 10^6$	0.34*
*24.35	12.	$16.63 \cdot 10^{-3}$	33.25 3.33	$0.67 \cdot 10^{-2}$	$*1.33 \cdot 10^7$ $*1.33 \cdot 10^6$	0.4*
*27.9	13.9	$65.81 \cdot 10^{-4}$	13.16 1.32			

Table 1. Integrated cross section σ_{int} in the range $|\cos\theta| \leq 0.8$ and number of counts, for $\overline{p} + p \rightarrow e^+ + e^-$, $\overline{p} + p \rightarrow \pi^+ + \pi^-$, corresponding to an integrated luminosity $\mathcal{L} = 2 \text{ fb}^{-1}$ (the second line at each s value corresponds to $\mathcal{L} = 0.2 \text{ fb}^{-1}$). For the values marked with a '*', the full simulation has not been performed for the background.

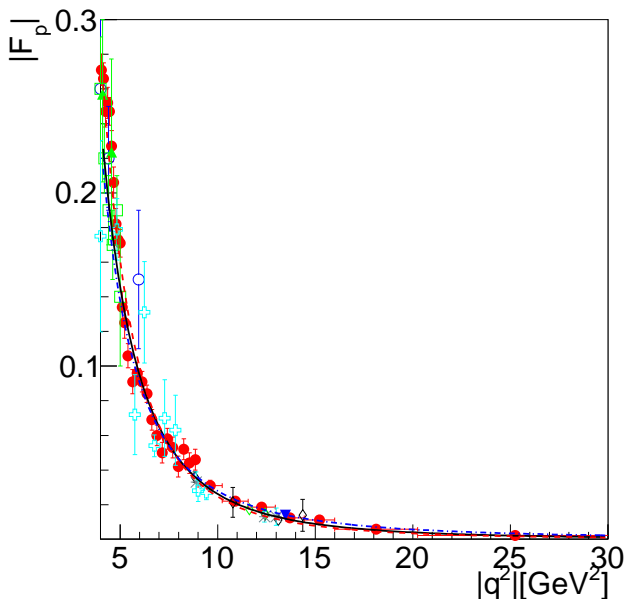


Fig. 1. (Color online) q^2 dependence of the world data for $\overline{p} + p \rightarrow e^+ + e^-$. The effective proton TL FF, $|F_P|$, is extracted from the annihilation cross sections assuming $|G_E| = |G_M|$: Fenice [7] (blue open circles); E835 [6, 5] (green open lozenge); PS170 [10] (gray open stars); E760 [9] (dark grey asterisk); DM1 [18] (green full triangles); DM2 [12, 11] (green open squares); BES [1] (cyan open cross); CLEO [33] (blue triangle down); BABAR [31, 30] (red full circles). Different parametrizations are shown from Eq. (10) (black solid and red dashed lines) and from Eq. (9) (blue dash-dotted line) (see text).

Fig. 2. (Color online) Angular distribution for the reaction $\overline{p} + p \rightarrow \pi^+ + \pi^-$, as a function of $\cos\theta$.

Therefore the generator uses two different parametrizations: in the "low" energy region, $p_{\overline{p}} < 5 \text{ GeV}/c$, ($p_{\overline{p}}$ is the antiproton beam momentum in the laboratory system) the parameters of Legendre polynomials up to the order of ten have been fitted to the data from Ref. [20]. In the "high" energy region $5 \leq p_{\overline{p}} < 12 \text{ GeV}/c$, the Regge inspired parametrization from Ref. [39], which was tuned on the data from Refs. [19, 15, 41, 8] was applied.

To be done For illustration, in Figs. 2 and 3 the differential and total cross sections for the reaction $\overline{p} + p \rightarrow \pi^+ + \pi^-$ are reported. The functions used in the pion generator are shown in comparison to a data sample.

The physics and background events can be produced by different event generators according to the physics case, such as EvtGen [28] which is used for generating benchmark reactions, and the Dual Parton Model [16] for the generic annihilation background in $\overline{p}p$ annihilation.

The EvtGen generator is used to generate the signal ($\overline{p}p \rightarrow e^+e^-$) and the background ($\overline{p}p \rightarrow \pi^+\pi^-$). The phase space PHSP model (flat distribution in $\cos\theta$) has also been used for acceptance studies. Taking into account that the ratio of cross sections $\sigma(\overline{p}p \rightarrow \pi^+\pi^-)/\sigma(\overline{p}p \rightarrow e^+e^-) \leq 10^6$, a number of $10^8(10^6)$ events are generated for the reaction $\overline{p}p \rightarrow \pi^+\pi^-(e^+e^-)$ at each value of the three incident antiproton momenta $p_{\overline{p}} = 1.7, 3.3$ and 6.4 GeV ($s = 5.4, 8.2, 13.9 \text{ GeV}^2$ respectively). Such statistics allows to optimize the kinematical cuts on the variables in such a way to eliminate all the pions, keeping an acceptable efficiency for the signal.

For the other values of Table 1 only the simulation for the signal was done, extrapolating the values of the

Fig. 3. (Color online) Total cross section for the reaction $\bar{p} + p \rightarrow \pi^+ + \pi^-$, as a function of the total energy squared, s .

final cuts on the kinematical variables found for the other settings. The events are generated in the full range of the polar angle θ and azimuthal angle ϕ .

3 The $\overline{\text{PANDA}}$ experiment

3.1 The $\overline{\text{PANDA}}$ detector

As mentioned above, the $\overline{\text{PANDA}}$ experiment is based on a broad physics programme which require 4π acceptance, high resolution and tracking capability, and excellent neutral and charged particle identification, photon detection from 3 MeV to 10 GeV in a high rate environment. The average interaction rate is expected to reach 20 MHz. The structure and the components of the detector have been optimized following the experience gained at high energy experiments. A detailed description of the subdetectors and their performances can be found in number of documents [32] and will not be repeated here. We will mention the characteristics of the detectors which play an important role in the FFs measurements. **revise the description of the detector with the same information for all - especially resolution** An overall picture of the detector is shown in Fig. 4. The size of the detector is about 12 m along the beam direction. It is a compact detector, with two magnets, a central solenoid and a forward dipole. The (pellet or jet) target is surrounded by the microvertex detector (MVD) [21]. The central tracker consists of straw tubes (STT) to insure a precise spatial reconstruction of the trajectories of charged particles in a broad momentum range from about a few 100 MeV/c up to 8 GeV/c through energy loss measurement dE/dx [22]. The DIRC (Detection of Internally Reflected Cerenkov) will be used for particle identification at polar angles between 22° and 140° , and momentum up to 5 GeV/c [17].

The barrel will be completed by an electromagnetic calorimeter (EMC), consisting of Lead Tungstate PbWO_4 crystals, to insure an efficient photon detection from 3 MeV to 10 GeV [26]. Besides the cylindrical barrel of 11360 crystals, a forward endcap (3856 crystals) and a backward endcap (600 crystals) are added. The light produced by each barrel crystal is read out by two rectangular Large Area Avalanche Photodiodes (LAAPD). The EMC will be operated at a temperature of $T = -25^\circ \text{C}$ to maximize the scintillation light.

Particles emitted at angles smaller than 22° will be detected by three planar stations of Gas Electron Multiplier (GEM) downstream of the target [13]. The muon identification will be done by Iarocci proportional tubes with scintillator counters placed outside and inside the solenoid and dipole magnets, in the inner gap of the solenoid yoke

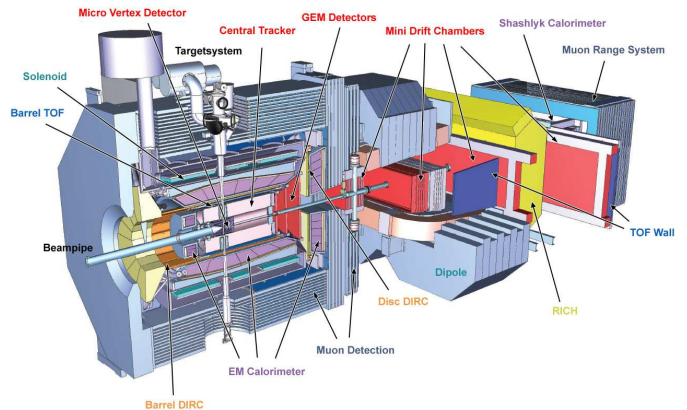


Fig. 4. (Color online) View of the $\overline{\text{PANDA}}$ detector.

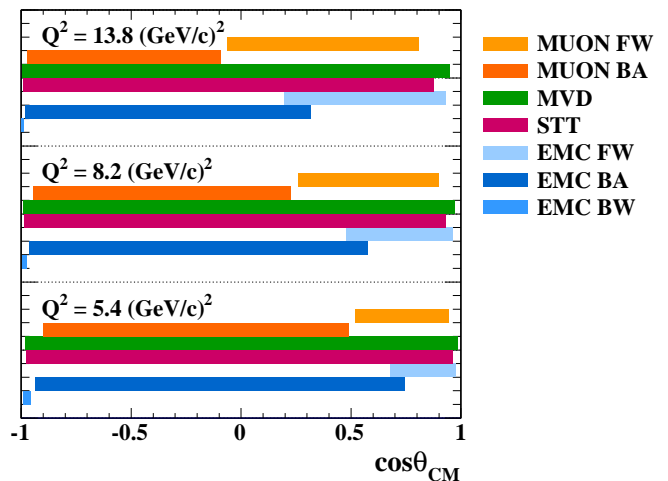


Fig. 5. (Color online) Acceptance for the relevant subdetectors as function of $\cos\vartheta$ in CM system. Add DIRC - $\theta_{\text{CM}} \rightarrow \vartheta$ in the legend- black and white figure.

and between the hadron calorimeter planes, with a forward angular coverage up to 60° (Reference?). The Detection of Internally Reflected Cerenkov light will be used for PID for particles with momenta of 0.8 GeV up to about 5 GeV, at polar angles between 22° and 140° (Barrel DIRC) (Reference?).

In Fig. 5 the geometrical acceptance of the subdetectors used in the analysis is shown as a function of the CM angle ϑ for three values of the total energy s , $s = 5.4, 8.2, 13.4 \text{ GeV}^2$. ϑ is defined as the angle between the direction of the \bar{p} momentum and the edge of the subdetector.

In order to collect different types of events a continuous data acquisition with fast readout followed by an intelligent software trigger is under development.

3.2 Simulation and analysis framework

The offline software for the $\overline{\text{PANDA}}$ detector simulation and event reconstruction is PANDARoot, which is the

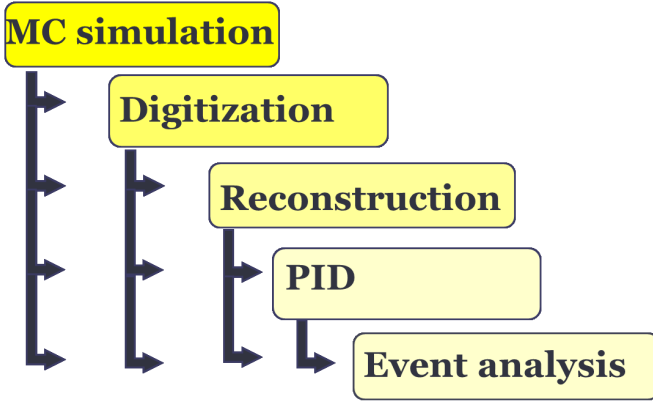


Fig. 6. Standard chain of reconstruction in PANDARoot.

common framework for the future FAIR experiments, FAIR-Root. The transport models GEANT3 and GEANT4 [2] are implemented in the software, based on ROOT [14] and Virtual MC [25] packages. Different reconstruction algorithms for tracking and PID are under development and optimization in order to achieve the requirements of the experiment. The different steps undergone by a simulation using the PANDARoot framework are illustrated in Fig. 6.

HERE ON TO BE UPDATED. STARTING FROM THIS POINT WE FOLLOW CLOSELY ALAA NOTE. THE RELEVANT SPECTRA SHOULD BE SELECTED AND EVENTUALLY REDRAWN.

3.3 Reconstructed PID variables

The most sensitive variable in the EMC that can be used for the identification of charged particles is the ratio of the energy deposit (E_{EMC}) on the reconstructed momentum as shown in Fig. 7. For the signal (Fig. 7 right), this ratio is distributed around a mean value of about 1, with a width of the order of ~ 0.1 . The discontinuities that appear on the plot are due to the transition regions between the different parts of the EMC. For the background (Fig. 7 left), the distribution shows a double structure: a narrow peak at low “ $E_{EMC}/\text{momentum}$ ” values, which is due to energy loss by ionization, and another one around $E_{EMC}/\text{momentum}=0.4$ corresponding to the hadronic interactions. The tail of the latter extends to much higher values, causing background under the electron peak.

The energy loss per unit of length dE/dx in the STT is shown in Fig. 8 as a function of the reconstructed momentum.

The Cherenkov angle provided by the Barrel DIRC is shown in Fig. 9. One can see that, at high energy, there is no possibility to disentangle electrons and pions using these two variables (dE/dx and θ_c).

For the electron/pion separation, one can apply cuts on the variables shown in Figs. 7, 8, and 9 (hard cuts).



Fig. 7. Energy loss in the EMC over the reconstructed momentum for a sample of reconstructed events of the background (left) and the signal (right), as a function of the reconstructed momentum (Lab system), obtained with PHSP model for $s=8.2 \text{ GeV}^2$.



Fig. 8. Same as Fig. 7 for the energy loss in the STT.

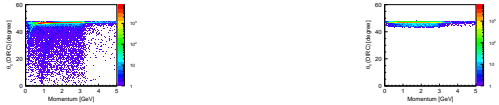


Fig. 9. Same as Fig. 7 for the Cherenkov angle of the Barrel DIRC.

However, with this method, a large fraction of the signal efficiency is lost. In the present analysis, PID cuts are rather applied on the probabilities given by the sub-detectors which are calculated on the basis of these variables.

3.3.1 PID probabilities

The probability for a detected particle to be identified as the signal is discussed here. The probability for a pion to be identified as an electron, given by the sub-detectors EMC, STT, Barrel and Disc DIRC and MVD are shown in Fig. 10 for positive (left) and negative (right) pions. The distributions are maximum at PID probability equal to zero where the pions are well identified. The peak at 0.2, is related to the events when the method used to calculate the probability can not provide a decision about the type of the particle. In this case, the probability is splitted equally into the five particle types. The EMC is the most important detector for the electron identification. **The figures should be redrawn as composite figures: LEFT the signal, RIGHT the background**



Fig. 10. PID probability given by the EMC (black), EMC+STT (green) and total probability from EMC,STT,MVD and DIRC (red), for π^+ to be identified as e^+ (left) and π^- to be identified as e^- (right) for $s=8.2 \text{ GeV}^2$.

The global PID, which combines the relevant information of all sub-detectors associated with one track, has been realized with a standard likelihood method. Based on the likelihoods obtained by each individual sub-detector, the probability for a track originating from a particle type $P(k)$ is evaluated as follows:

$$P(k) = \frac{\prod_i P_i(k)}{\sum_j \prod_i P_i(j)} \quad (11)$$

where the product with index i runs over all considered sub-detectors and the sum with index j runs over the five particle types. In order to enhance the rejection power of the background one should apply PID cuts, not only to the combined probability, but also on the individual probabilities P_i in order to eliminate the events with corresponding $P_i \sim 0$.

For the signal, the PID probabilities are shown in Fig. 11. The distributions have their maximum at PID probability equal to one. These plots show that the combined probability increases the efficiency of the signal as expected from Eq. 11.



Fig. 11. PID probability given by the EMC (black), EMC+STT (green) and total probability (red), for e^+ to be identified as e^+ (left) and e^- to be identified as e^- (right), for $s=8.2 \text{ GeV}^2$.

3.3.2 Number of fired crystals in the EMC

The number of fired crystals in the EMC (N_{EMC}) is also an important parameter which can be used for electron/pion separation. This variable is not taken into account by the Bayes PID probability calculated for the EMC and it depends on the kinematics of the reaction. Fig. 12 shows that a large fraction of the background events corresponds to less than 5 fired crystals, while the signal has a maximum in the region of $N_{EMC} > 5$.



Fig. 12. Number of fired crystals in the EMC, for a sample of reconstructed events of the background (left) and the signal (right), for positive (black) and negative (red) particles, for $s=8.2 \text{ GeV}^2$.

4 Analysis

The events for both channels have been analysed in two steps:



Fig. 13. Angular distribution in the CM system for a sample of reconstructed events of the background (left) and the signal (right), for positive (black) and negative (red) particles, obtained with PHSP model for $s=8.2 \text{ GeV}^2$.

- First, the events which have one positive and one negative particle are selected. In the case when the track contains more than one positive or one negative particle (secondary particles which may be produced by the interaction of generated primary particles with the detector materials), the pair (one positive + one negative) which is the best back-to-back in the CM system is selected.
- Then, the reconstructed variables (kinematics, PID probabilities,...) of the selected events are analyzed and the best cuts which can suppress the pion background keeping at the same time the best possible efficiency for the signal are set.

4.1 Kinematical variables

The CM angular distribution for the selected events before the cuts, is illustrated in Fig. 13 for the background (left) and the signal (right). **Compared to the MC events, a fraction of about 82% (84 %) for the background (signal) is reconstructed and selected. The loss of $\approx 20\%$ corresponds mostly to forward and backward events ($\cos\theta \sim \pm 1$) due to the acceptance of the PANDA detector.**

Fig. 14 shows the distribution in ϕ -angle for the electron and pion pairs. The azimuthal angles (ϕ for the negative and ϕ' for the positive particle) do not depend on the Lorentz transformation (the same in the CM and Lab system).



Fig. 14. The difference $|\phi - \phi'|$ for a sample of reconstructed events of the pion (left) and the electron (right) pairs, for $s=8.2 \text{ GeV}^2$.

Unlike the momentum and energy of a charged particle, the polar angles (θ for the negative and θ' for the positive particle in CM system) as well as the azimuthal angles, in average are not affected by the Bremsstrahlung emission during the travel of the particle through the detector.

The reconstructed invariant mass (of the two charged pions and electrons) is defined as:

$$M_{inv} = \sqrt{(k_1 + k_2)^2}, \quad (12)$$

where k_1 and k_2 are the reconstructed four momenta of the negative and positive pions (or electrons) in the final state. The reconstructed invariant mass is shown in Fig. 15 for $s=8.2 \text{ GeV}^2$. The distribution has a maximum at the theoretical value of $\sqrt{s} \approx 2.86 \text{ GeV}$.



Fig. 15. The invariant mass for a sample of reconstructed pion (left) and electron (right) pairs, for $s=8.2 \text{ GeV}^2$.

4.2 PID probability and kinematical cuts

The cuts applied to the background and the signal events are reported in Tab. 2, for each value of the momentum transfer squared ($s = 5.4, 8.2$ and 13.9 GeV^2). The cuts are adjusted in order to kill the 3×10^8 events of the background, keeping at the same time the best possible values of the signal efficiency. The additional effect of the individual cut are reported for $s = 8.2 \text{ GeV}^2$ in Tab. 3.

The reconstructed events for the signal, after applying the cuts, as well as the original MC events are shown in Fig. 16 (left) for $s=8.2 \text{ GeV}^2$. The drop of reconstructed events at $\cos\theta = 0.65$ ($\theta_{lab} \sim 22.3^\circ$) is due to the transition region between the forward and the barrel EMC (Fig. 16 right).

5 Expected statistical error on the proton FF ratio

From this point we performed two parallel analysis to determine the efficiency, which drives the statistical error on the FFs.

5.1 Analysis I

The reconstructed electron events, after the suppression of the whole $\pi^+\pi^-$ background, are used to extract the statistical error on the proton FF ratio. A number $M = 10^6$ of Monte Carlo events are generated for the reaction $\overline{p}p \rightarrow e^+e^-$, at the incident antiproton momentum $p=3.3 \text{ GeV}$ using the PHSP model.

5.1.1 Extraction of the signal efficiency

The signal efficiency was extracted from the PHSP events for each $\cos\theta$ bin. The ratio between the PHSP reconstructed $R(c)$ (after the cuts), and the MC $M(c)$ events represents the signal efficiency as a function of the angular distribution (Figs. 17, 18), which can be written as:

$$\epsilon(c) = \frac{R(c)}{M(c)}, \quad c = \cos\theta. \quad (13)$$

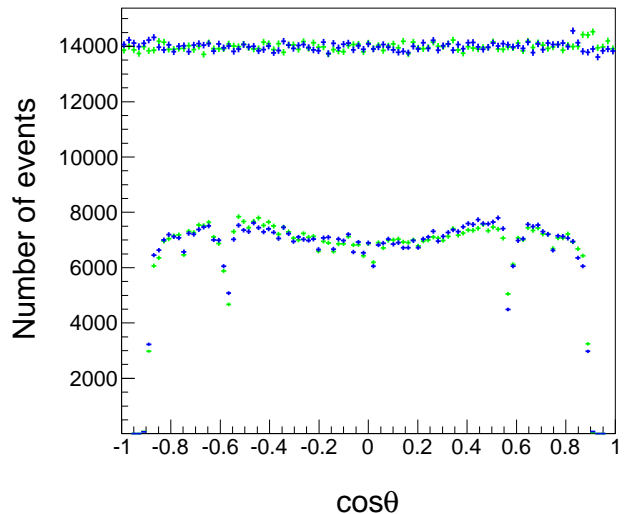


Fig. 16. Angular distribution (left) of e^- (blue) and e^+ (green) in the CM system, for the MC events (top) and the reconstructed events after the cuts (bottom) obtained with PHSP model for $s=8.2 \text{ GeV}^2$.

$s [\text{GeV}^2]$	5.4	8.2	13.9
$\epsilon[\%]$	54.36	51.9	43.8

Table 4. Efficiency integrated over the angular range $|\cos\theta| \leq 0.8$ for different s values.

To the content of each bin of the MC and reconstructed events, is attributed the error $\Delta M(c) = \sqrt{M(c)}$ and $\Delta R(c) = \sqrt{R(c)}$ respectively. The error on the efficiency is derived using Eq. 13 as follows:

$$\Delta\epsilon(c) = \sqrt{\frac{\epsilon(c)(1 + \epsilon(c))}{M(c)}} \quad (14)$$

Eq. 14 shows that, the statistical error on the efficiency depends on the number of MC events and it can be reduced to very small values.

Due to the drop of the efficiency in the region $\cos\theta > 0.8$, the analysis for the extraction of the proton FF ratio is limited to the angular range $\cos\theta = [-0.8, 0.8]$. The integrated efficiency in this region is given by Tab. 4 for the considered $s = q^2$ values.

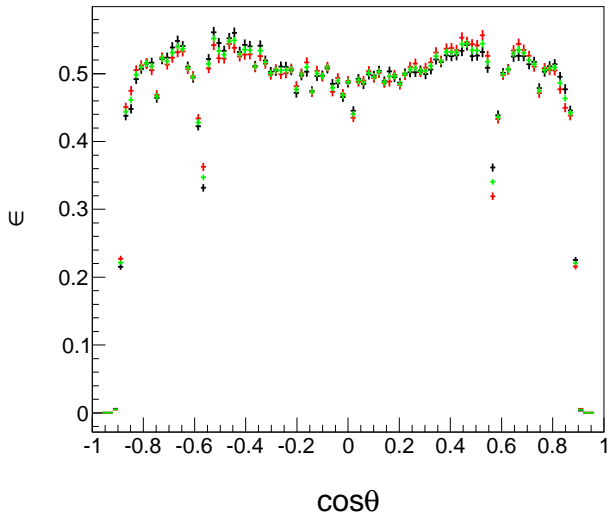
5.1.2 Physical events

The PHSP events which have a flat distribution of $\cos\theta$ in CM system, do not contain the physics of the proton FFs. Physical events follow the angular distribution of Eq. 3. Therefore the Monte Carlo histograms are rescaled by the weight $\omega(c) = 1 + \mathcal{A} \cos^2\theta$, where \mathcal{A} is given according to a model for G_M and G_E . The advantage of the PHSP model is that the same simulation can be used to test different models of the proton FFs at a fixed energy.

$s[\text{GeV}^2]$	5.4	8.2	13.9
Combined PID probability	> 0.99	> 0.99	> 0.999
Individual PID_i	> 0.05	> 0.05	> 0.06
N_{EMC}	> 5	> 5	> 5
$\theta + \theta'$	$[178^\circ, 182^\circ]$	$[178^\circ, 182^\circ]$	$[175^\circ, 185^\circ]$
$ \phi - \phi' $	$[178^\circ, 182^\circ]$	$[178^\circ, 182^\circ]$	$[175^\circ, 185^\circ]$
Invariant mass [GeV]	no cut	> 2.14	> 2.5

Table 2. PID probability and kinematical cuts applied to the electron and pion reconstructed events.

Cut	pions [events]	Integrated efficiency
$\text{PID}^{tot} > 0.99, \text{PID}_i > 0.05$	693	61%
$N_{EMC} > 5$	268	60%
Kinematical cuts (θ, ϕ)	9	51%
$\sqrt{s} > 2$ [GeV]	3, $[-0.8, 0.8]=1$	46%, $[-0.8, 0.8] = 54\%$
$\sqrt{s} > 2.135$ [GeV]	0	44%, $[-0.8, 0.8] = 51.9\%$

Table 3. Number of events after the PID probability and the kinematical cuts for the signal and the background, for $s=8.2$ GeV^2 .**Fig. 17.** Signal efficiency for e^- (red), e^+ (black) and for their mean (green), obtained with PHSP model for $s=8.2$ GeV^2 .**Fig. 18.** Same as Fig. 17 for $s = 5.4$ GeV^2 (left) and $s = 13.9$ GeV^2 (right).

One can note that the simulation should not show any difference between electrons and positrons. Being a binary process, in absence of odd contributions in the am-

plitudes¹ the detection of an electron at a definite value of $c = \cos \theta$ is equivalent to the detection of a positron at $\cos(\pi - \theta)$.

In the real experiment, however, the efficiency spectra will have to be evaluated on the experimental spectra, because experimental asymmetries, not included in the present 'ideal' situation, are likely to appear. For this analysis, we can safely sum e^+ and e^- MC generated events, in order to gain statistics and reduce even further the uncertainty on the efficiency.

Fig. 19 shows the angular distribution of the Monte Carlo PHSP $M(c)$ events and physical $P(c)$ events, at $s=8.2$ GeV^2 , for the case:

$$R = \frac{|G_E|}{|G_M|} = 1, \quad \mathcal{A} = \frac{\tau - 1}{\tau + 1}. \quad (15)$$

The signal efficiency estimated following the PHSP events is applied to $P(c)$ to obtain the physical reconstructed events $W(c)$:

$$W(c) = P(c)\epsilon(c), \quad c = \cos \theta. \quad (16)$$

5.1.3 Normalization: observed events

The physical events $W(s)$ after the cuts are normalized according to the integrated counting rate given by Tab. 1 which depends on the energy of the system and the luminosity of the experiment. The events which will be observed in the real experiment are estimated (with a luminosity of $\mathcal{L} = 2 \text{ fb}^{-1}$) as follow:

$$O(c) = W(c) \cdot \frac{N_E[-0.8, 0.8]}{\int_{-0.8}^{0.8} P(c)dc}, \quad c = \cos \theta, \quad (17)$$

¹ This is the case of the present simulation: we will assume one photon exchange, and the photon emission, calculated with the PHOTOS package does not induce any asymmetry [40].

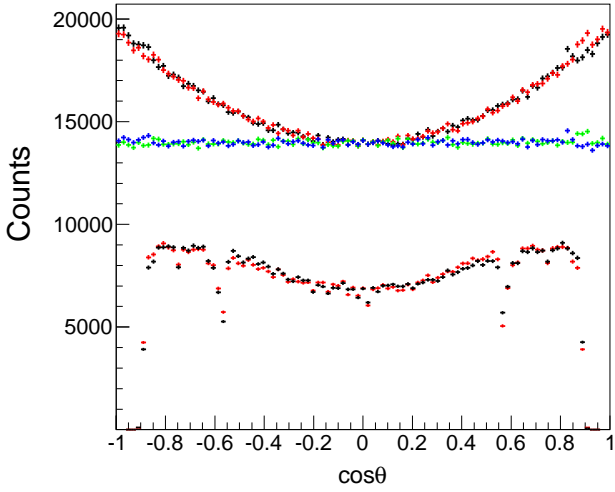


Fig. 19. Angular distribution of the MC events obtained with PHSP model for e^- (blue) and e^+ (green) in the CM system, and following physical distribution (e^- (black) and e^+ (red)), before (top) and after the reconstruction the cuts (bottom), for $s = 8.2 \text{ GeV}^2$ and $R = 1$.

with an error $\Delta O(c) = \sqrt{O(c)}$ since the experimental error will be finally given by the accumulated statistics of the detected events. N_E is the number of Monte Carlo events

5.1.4 Efficiency correction and fit

The fit procedure is applied on the observed events after the correction of the efficiency, $F(c)$:

$$F(c) = O(c)/\epsilon(c), \quad \Delta F(c) = \Delta O(c)/\epsilon(c) = \sqrt{O(c)}/\epsilon(c), \quad (18)$$

where the error on the efficiency $\Delta\epsilon(c)$ is neglected. For each s value, the distribution $F(c)$ as a function of $\cos^2\theta$ is fitted with a two-parameter function (straight line). The linear fit function is:

$$y = a_0 + a_1x, \quad \text{with } x = c^2, \quad a_0 \equiv \sigma_0, \quad a_1 \equiv \sigma_0\mathcal{A}, \quad (19)$$

where a_0 and a_1 are the parameters to be determined by minimization. They are related to the physical FFs, through Eqs. (4). The observed events, before ($O(c)$) and after ($F(c)$) efficiency correction are shown in Figs. 20 and 21.

The measurement of the angular asymmetry allows one to determine the FF ratio through the relation:

$$R = \sqrt{\tau \frac{1 - \mathcal{A}}{1 + \mathcal{A}}} \quad (20)$$

In the limit of small errors, as long as first order statistical methods work, the error on R can be obtained from

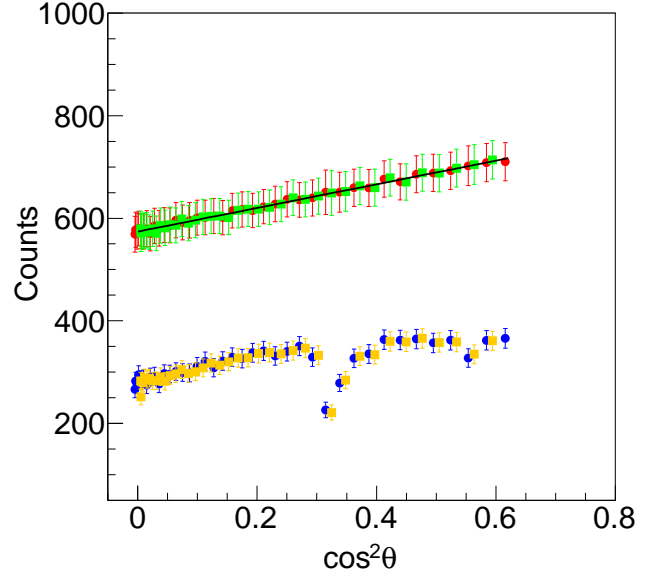


Fig. 20. Observed events before efficiency correction $O(c)$ (forward events (blue circles) and backward events (orange squares)) and after efficiency correction $F(c)$ (forward events (red circles) and backward events (green squares)), as a function of $\cos^2\theta$ for $s = 8.2 \text{ GeV}^2$ and $R = 1$. The line is the linear fit.



Fig. 21. Same as Fig. 20 but for $s = 5.4 \text{ GeV}^2$ (left) and $s = 13.9 \text{ GeV}^2$ (right). The lines are the linear fit.

standard error propagation on \mathcal{A} :

$$\Delta R = \frac{1}{R} \frac{\tau}{(1 + \mathcal{A})^2} \Delta \mathcal{A}. \quad (21)$$

The result of the fit are reported in Tab. 5. The input values of R and \mathcal{A} are recovered within the error ranges.

$s \text{ [GeV}^2\text{]}$	R	\mathcal{A}	$R \pm \Delta R$	$\mathcal{A} \pm \Delta \mathcal{A}$
5.4	1	0.21	0.992 ± 0.009	0.218 ± 0.009
8.2	1	0.4	0.997 ± 0.045	0.401 ± 0.038
13.9	1	0.59	1 ± 0.396	0.595 ± 0.255

Table 5. Expected statistical errors on the angular asymmetry and the proton FF ratio, for different s values. The second and the third columns are the theoretical values (simulation inputs). The fourth and the fifth columns are the results of the fit. The statistical errors are extracted in the angular range $|\cos\theta| \leq 0.8$.

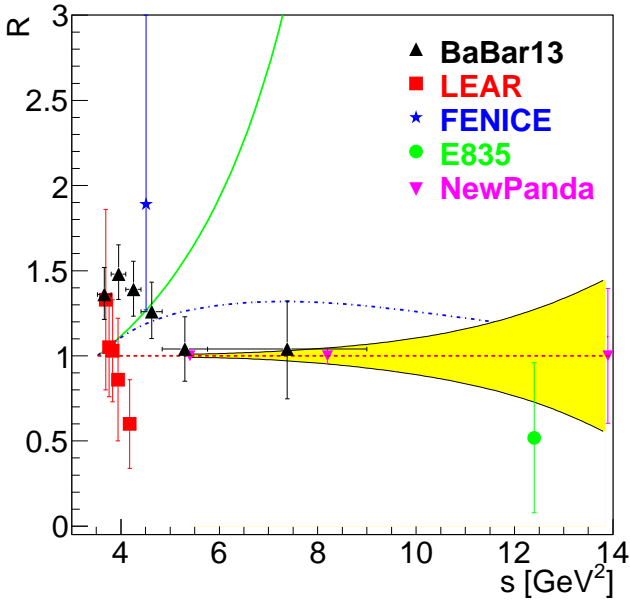


Fig. 22. Expected statistical precision on the determination of the proton FF ratio for $R=1$, from Ref. [36] (yellow dashed band) and from the present simulation (black triangles) as a function of $s = q^2$, compared with the existing data. The statistical errors are extracted in the angular range $|\cos\theta| \leq 0.8$. Curves are theoretical predictions.

The three points obtained from the present simulations and the world data on the proton FF ratio are shown in Fig. 22 for $R = 1$ and Fig. 23 for the different values of R predicted by theoretical models. Data are from Ref. [10] (red squares), from Ref. [29] (black triangles), from Ref. [5] (green circles), and from Ref. [7] (blue stars). The yellow band is the result obtained in the previous analysis [36] within the BaBar framework. The curves are theoretical prediction from vector dominance model (solid green line), from extended Gary-Kruempfelmann (blue dash-dotted) and from naive quark model (red dashed line) model.

6 Extrapolation and projected data

The real efficiency will be determined during the experiment using the physics events, so that we will not have to extrapolate the results from the Monte Carlo, which contains ingredients and cuts to be adjusted on the data themselves. Moreover, the counting rates (i.e., the cross sections) are also affected by an uncertainty: different models give different values, especially at large s , where they are not so constrained by the data). The experimental error depends on the square root of the efficiency. Let us show here the dependence of the error on the number of points, on the ratio R and on the asymmetry A as a function of the integrated efficiency.

Fig. 24 shows the integrated efficiencies for $q^2 = 5.4, 8.2$ and 13.9 GeV^2 over the angular range $|\cos\theta| \leq 0.8$. The

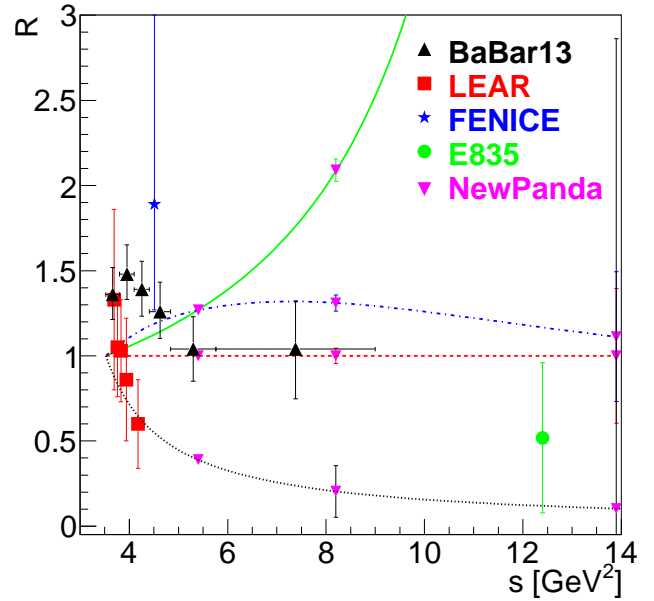


Fig. 23. Same as Fig. 22 but for different values of R according to the theoretical predictions.

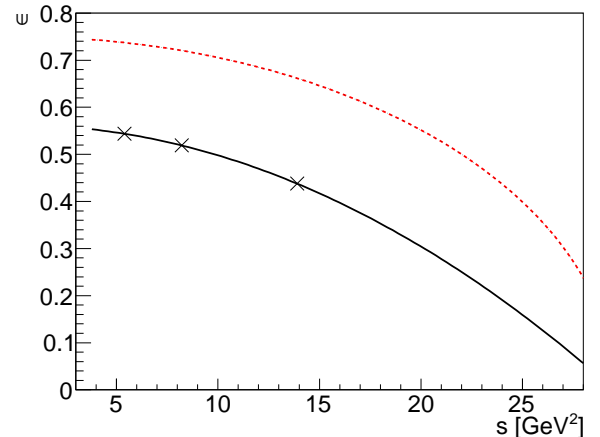


Fig. 24. Integrated efficiency of the signal $\bar{p}p \rightarrow e^+e^-$ as a function of s .

curve is obtained by extrapolation of the efficiency points obtained from the present simulation.

The experimental situation for the generalized proton FF, F_p , which can be extracted from the TL cross section 6, in the hypothesis $|G_E| = |G_M|$ and using the dipole parametrization for the magnetic FF (Eq. 10), is shown together with the world data in Fig. 25.

7 Statistical errors on G_E and G_M

In order to extract the FF ratio, the measurement of the slope of the linear distribution of the cross section as a

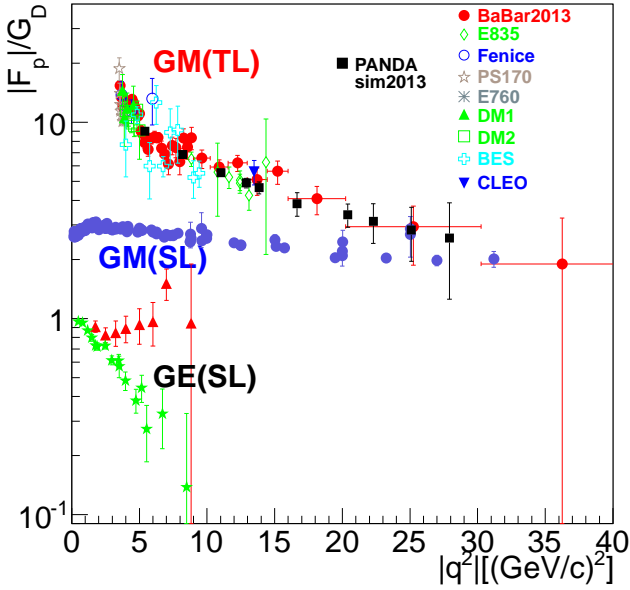


Fig. 25. q^2 -dependence of the world data on the effective proton time-like (TL) FFs, as extracted from the annihilation cross section assuming $|G_E| = |G_M|$. The errors obtained or extrapolated from the present simulation, for an integrated luminosity of 2 fb^{-1} , are shown with the black squares. Each point corresponds to four months of data taking.

function of $\cos\theta$ is sufficient. To obtain the individual errors and the values of G_E and G_M , one needs to know the absolute normalization². The normalization needs an absolute luminosity measurement, which will be known with one percent precision.

For the individual determination of $|G_E|$ and $|G_M|$, we use a two parameter fit (a and b) to extract $|G_E|$ and $|G_M|$ from the form based on Eqs. (4) on the histograms of the events after the efficiency correction (which are defined in section 5.1.4):

$$y = a + b \cos^2 \theta \quad (22)$$

where $|G_E|$ and $|G_M|$ are extracted from $a \equiv \sigma_0$ and $b \equiv \sigma_0 \mathcal{A}$ by

$$|G_M|^2 = \frac{\sigma_0}{2\mathcal{N}}(1 + \mathcal{A}); \quad |G_E|^2 = \tau \frac{\sigma_0}{2\mathcal{N}}(1 - \mathcal{A}); \quad (23)$$

and their errors:

$$\begin{aligned} \Delta|G_M|^2 &= \frac{1}{2\mathcal{N}} \sqrt{(1 + \mathcal{A})^2 \Delta\sigma_0 + (\sigma_0 \Delta\mathcal{A})^2}; \\ \Delta|G_E|^2 &= \frac{\tau}{2\mathcal{N}} \sqrt{(1 - \mathcal{A})^2 \Delta\sigma_0 + (\sigma_0 \Delta\mathcal{A})^2}; \end{aligned} \quad (24)$$

Adding a relative error on the normalization factor: $\Delta\mathcal{N}/\mathcal{N} = 0.02$, we find:

$$\Delta|G_M|^2 = \frac{1}{2\mathcal{N}} \sqrt{(1 + \mathcal{A})^2 \Delta\sigma_0 + (\sigma_0 \Delta\mathcal{A})^2 + |G_M|^2 \left(\frac{\Delta\mathcal{N}}{\mathcal{N}}\right)^2};$$

² Note, however, that a combined analysis of q^2 and θ dependence, if a complete set of data will be available, will bring a more consistent information.

$$\Delta|G_E|^2 = \frac{\tau}{2\mathcal{N}} \sqrt{(1 - \mathcal{A})^2 \Delta\sigma_0 + (\sigma_0 \Delta\mathcal{A})^2 + |G_E|^2 \left(\frac{\Delta\mathcal{N}}{\mathcal{N}}\right)^2} \quad (25)$$

The statistical error on the FF ratio, can be derived:

$$R = \frac{|G_E|}{|G_M|}, \quad \Delta R = R \sqrt{\left(\frac{\Delta|G_E|}{|G_E|}\right)^2 + \left(\frac{\Delta|G_M|}{|G_M|}\right)^2} \quad (26)$$

The result of the fit are reported in Tab. 6. The input values of $|G_M| = |G_E|$ (Eq. 10) are recovered within the error ranges.

8 Conclusion

A full simulation has been performed within the PANDA-Root framework for three kinematical points, where 3×10^6 events have been simulated for the signal ($\bar{p}p \rightarrow e^+e^-$) and 3×10^8 events for the background ($\bar{p}p \rightarrow \pi^+\pi^-$). In comparison to the previous analysis [36], the description of the detector is more realistic as well as the different steps of reconstruction and analysis. The efficiency has improved by 5 to 10 %, although the experimental cuts will be finally set on the real data.

The knowledge of the TL electromagnetic FFs will be extended in a large kinematical range. The present results show that the statistical error at $q^2 \geq 14 \text{ GeV}^2$ will be comparable to the one obtained by BaBar at 7 GeV^2 . Note that the results obtained in this work will be improved with the continuing development of the PANDA-Root software.

The study of the precision of the determination of the individual FFs shows that a meaningful precision can be obtained, assuming a 2% precision on the absolute normalization. The absolute cross section measurement depends essentially on the precision achieved in the luminosity measurement.

9 Acknowledgments

Thanks are due to E. Fioravanti and P. Buehler, for essential help during the analysis. One of us (ETG) thanks the HIM (Mainz) for kind hospitality during the completion of this work.

References

1. M. Ablikim et al. Measurement of the cross section for $e^+e^- \rightarrow p\bar{p}$ at center-of-mass energies from 2.0-GeV to 3.07-GeV. *Phys.Lett.*, B630:14–20, 2005.
2. S. et al. Agostinelli. Geant4a simulation toolkit. *Nuclear Instruments and Methods in Physics Research Section A: Accelerators, Spectrometers, Detectors and Associated Equipment*, 506(3):250 – 303, 2003.
3. A.I. Akhiezer and Mikhail.P. Rekalov. Polarization phenomena in electron scattering by protons in the high energy region. *Sov.Phys.Dokl.*, 13:572, 1968.

s [GeV ²]	$ G_M = G_E $	$ G_M \pm \Delta G_M $	$ G_E \pm \Delta G_E $	$R \pm \Delta R$
5.4	0.1215	0.1218 ± 0.0013	0.1208 ± 0.0014	0.993 ± 0.007
8.2	0.0435	0.0435 ± 0.0006	0.0433 ± 0.0017	0.997 ± 0.039
13.9	0.0110	0.0110 ± 0.0007	0.0109 ± 0.004	0.997 ± 0.375

Table 6. Expected statistical errors on the proton FFs, for different s values. The second column is the theoretical value (simulation input). The third, fourth and the fifth columns are the results of the fit. The statistical errors are extracted in the angular range $|\cos\theta| \leq 0.8$.

4. A.I. Akhiezer and Mikhail.P. Rekalov. Polarization effects in the scattering of leptons by hadrons. *Sov.J.Part.Nucl.*, 4:277, 1974.
5. M. Ambrogiani et al. Measurements of the magnetic form-factor of the proton in the timelike region at large momentum transfer. *Phys.Rev.*, D60:032002, 1999.
6. M. Andreotti, S. Bagnasco, W. Baldini, D. Bettoni, G. Borreani, et al. Measurements of the magnetic form-factor of the proton for timelike momentum transfers. *Phys.Lett.*, B559:20–25, 2003.
7. A. Antonelli, R. Baldini, P. Benasi, M. Bertani, M.E. Bigagini, et al. The first measurement of the neutron electromagnetic form-factors in the timelike region. *Nucl.Phys.*, B517:3–35, 1998.
8. T.A. Armstrong et al. Backward scattering in $\pi^- p \rightarrow p p i^-$, $\bar{p} p \rightarrow \pi^+ \pi^-$, $K^- p \rightarrow p K^-$ and $\bar{p} p \rightarrow p \bar{p}$ at 8-GeV/c and 12-GeV/c. *Nucl.Phys.*, B284:643, 1987.
9. T.A. Armstrong et al. Measurement of the proton electromagnetic form-factors in the timelike region at 8.9-GeV²–13 GeV². *Phys.Rev.Lett.*, 70:1212–1215, 1993.
10. G. Bardin, G. Burgun, R. Calabrese, G. Capon, R. Carlin, et al. Determination of the electric and magnetic form-factors of the proton in the timelike region. *Nucl.Phys.*, B411:3–32, 1994.
11. D. Bisello et al. Baryon pair production in $e^+ e^-$ annihilation at $\sqrt{s} = 2.4$ GeV. *Z.Phys.*, C48:23–28, 1990.
12. D. Bisello, S. Limentani, M. Nigro, L. Pescara, M. Posocco, et al. A Measurement of $e^+ e^- \rightarrow \bar{p} p$ for 1975-MeV $\leq \sqrt{s} \leq$ 2250-MeV. *Nucl.Phys.*, B224:379, 1983.
13. F.V. Bohmer, H. Angerer, S. Dorheim, C. Hoppner, B. Ketzer, et al. A continuously running high-rate GEM-TPC for PANDA. *Nucl.Phys.Proc.Suppl.*, 215:278–280, 2011.
14. Rene Brun and Fons Rademakers. {ROOT} an object oriented data analysis framework. *Nuclear Instruments and Methods in Physics Research Section A: Accelerators, Spectrometers, Detectors and Associated Equipment*, 389(12):81 – 86, 1997. New Computing Techniques in Physics Research V.
15. T. Buran, A. Eide, P. Helgaker, P. Lehmann, A. Lundby, et al. Anti-Proton-Proton Annihilation Into $\pi^+ \pi^-$ and $K^+ K^-$ at 6.2-GeV/c. *Nucl.Phys.*, B116:51, 1976.
16. A. Capella, U. Sukhatme, C-I Tan, and J. Tran Thanh Van. Dual parton model. *Phys.Rept.*, 236:225–329, 1994.
17. E.N. Cowie, A. Britting, A. Clarkson, V.KH. Dodokhof, M. Duren, et al. A focussing disc DIRC for PANDA. *Nucl.Instrum.Meth.*, A639:181–184, 2011.
18. B. Delcourt, I. Derado, J.L. Bertrand, D. Bisello, J.C. Bizot, et al. Study of the Reaction $e^+ e^- \rightarrow p \bar{p}$ in the Total Energy Range 1925 - 2180 MeV. *Phys.Lett.*, B86:395, 1979.
19. A. Eide, P. Lehmann, A. Lundby, C. Baglin, P. Briandet, et al. Elastic scattering and two-body annihilations at 5 gev/c. *Nucl.Phys.*, B60:173–220, 1973.
20. E. Eisenhandler, W.R. Gibson, C. Hojvat, P.I.P. Kalmus, L.C.Y. Lee Chi Kwong, et al. Measurement of Differential Cross-Sections for anti-Proton-Proton Annihilation Into Charged Pion and Kaon Pairs Between 0.79-GeV/c and 2.43-GeV/c. *Nucl.Phys.*, B96:109, 1975.
21. W. Erni et al. Technical Design Report for the: PANDA Micro Vertex Detector. 2012.
22. W. Erni et al. Technical design report for the PANDA (AntiProton Annihilations at Darmstadt) Straw Tube Tracker. *Eur.Phys.J.*, A49:25, 2013.
23. Maria Carmen Mora Espi. *Feasibility studies for accessing nucleon structure observables with the PANDA experiment at the future FAIR facility*. PhD thesis, Johannes Gutenberg-Universitt, 2012.
24. Robert Hofstadter. Electron scattering and nuclear structure. *Rev.Mod.Phys.*, 28:214–254, 1956.
25. I. Hrivnacova, D. Adamova, V. Berejnoi, R. Brun, F. Carminati, A. Fasso, E. Futo, A. Gheata, I. Gonzalez Caballero, A. Morsch, and for the ALICE Collaboration. The virtual monte carlo. 2003.
26. M. Kavatsyuk et al. Performance of the prototype of the electromagnetic calorimeter for PANDA. *Nucl.Instrum.Meth.*, A648:77–91, 2011.
27. E.A. Kuraev, E. Tomasi-Gustafsson, and A. Dbeysi. A Model for space and time-like proton (neutron) form factors. *Phys.Lett.*, B712:240–244, 2012.
28. David J. Lange. The evtgen particle decay simulation package. *Nuclear Instruments and Methods in Physics Research Section A: Accelerators, Spectrometers, Detectors and Associated Equipment*, 462(12):152 – 155, 2001. BEAUTY2000, Proceedings of the 7th Int. Conf. on B-Physics at Hadron Machines.
29. J.P. Lees et al. Measurement of the $e^+ + e^- \rightarrow p + \bar{p}$ cross section in the energy range from 3.0 to 6.5 GeV. Technical report, BaBar, 2013.
30. J.P. Lees et al. Study of $e^+ + e^- \rightarrow p + \bar{p}$ via initial-state radiation at BABAR. *Phys.Rev.*, D87:092005, 2013.
31. J.P. et al. Lees. Production of charged pions, kaons and protons in $e^+ e^-$ annihilations into hadrons at $\sqrt{s} = 10.54$ GeV. *Phys.Rev.*, D88:032011, 2013.
32. M.F.M. Lutz et al. Physics Performance Report for PANDA: Strong Interaction Studies with Antiprotons. 2009.
33. T.K. Pedlar et al. Precision measurements of the time-like electromagnetic form-factors of pion, kaon, and proton. *Phys.Rev.Lett.*, 95:261803, 2005.
34. D.V. Shirkov and I.L. Solovtsov. Analytic model for the QCD running coupling with universal alpha-s (0) value. *Phys.Rev.Lett.*, 79:1209–1212, 1997.

35. N.A. Stein, R.M. Edelstein, D.R. Green, H.J. Halpern, E.J. Makuchowski, et al. Comparison of the Line Reversed Channels $\bar{p}p \rightarrow \pi^- \pi^+$ and $\pi^+ p \rightarrow p \pi^+$ at 6-GeV/c. *Phys.Rev.Lett.*, 39:378–381, 1977.
36. M. Sudol, M.C. Mora Espi, E. Becheva, J. Boucher, T. Hennino, et al. Feasibility studies of the time-like proton electromagnetic form factor measurements with PANDA at FAIR. *Eur.Phys.J.*, A44:373–384, 2010.
37. E. Tomasi-Gustafsson and M.P. Rekalo. Search for evidence of asymptotic regime of nucleon electromagnetic form-factors from a compared analysis in space- and time- like regions. *Phys.Lett.*, B504:291–295, 2001.
38. Egle Tomasi-Gustafsson and Michail P. Rekalo. New possibility for further measurements of nucleon form factors at large momentum transfer in time-like region: $\bar{p} + p \rightarrow \ell^+ + \ell^-$, $\ell = e$ or μ . Technical report, CEA-Saclay, 2008.
39. Jacques Van de Wiele and Saro Ong. Regge description of two pseudoscalar meson production in antiproton-proton annihilation. *Eur.Phys.J.*, A46:291–298, 2010.
40. Z. Was, P. Golonka, and G. Nanava. PHOTOS Monte Carlo and its theoretical accuracy. *Nucl.Phys.Proc.Suppl.*, 181-182:269–274, 2008.
41. C. White, R. Appel, D.S. Barton, G. Bunce, A.S. Carroll, et al. Comparison of 20 exclusive reactions at large t. *Phys.Rev.*, D49:58–78, 1994.
42. Ulrich Wiedner. Future Prospects for Hadron Physics at PANDA. *Prog.Part.Nucl.Phys.*, 66:477–518, 2011.
43. ”Zambrana, M. et al. ”analysis of time-like form factor measurements at panda”. Technical report, HIM Mainz, 2014.
44. A. Zichichi, S.M. Berman, N. Cabibbo, and Raoul Gatto. Proton anti-proton annihilation into electrons, muons and vector bosons. *Nuovo Cim.*, 24:170–180, 1962.